

# Mechanistic Studies of Water Electrolysis and Hydrogen Electro-Oxidation on High Temperature Ceria-Based Solid Oxide Electrochemical Cells

Chunjuan Zhang,<sup>†,‡,¶</sup> Yi Yu,<sup>†,‡,¶</sup> Michael E. Grass,<sup>‡,¶</sup> Catherine Dejoie,<sup>‡</sup> Wuchen Ding,<sup>§</sup> Karen Gaskell,<sup>†</sup> Naila Jabeen,<sup>‡</sup> Young Pyo Hong,<sup>‡</sup> Andrey Shavorskiy,<sup>‡</sup> Hendrik Bluhm,<sup>‡</sup> Wei-Xue Li,<sup>§</sup> Gregory S. Jackson,<sup>†</sup> Zahid Hussain,<sup>‡</sup> Zhi Liu,<sup>\*,‡,||</sup> and Bryan W. Eichhorn<sup>\*,†</sup>

<sup>†</sup>Department of Chemistry and Biochemistry and Department of Mechanical Engineering, University of Maryland, College Park, Maryland 20742, United States

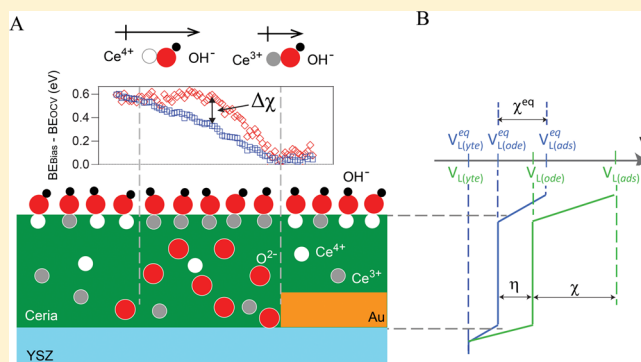
<sup>‡</sup>Lawrence Berkeley National Laboratory, Berkeley, California 94720, United States

<sup>§</sup>State Key Laboratory of Catalysis, Dalian Institute of Chemical Physics, Chinese Academy of Sciences, Dalian 116023, China

<sup>||</sup>School of Physical Science and Technology, ShanghaiTech University, Shanghai 200031, China

## Supporting Information

**ABSTRACT:** Through the use of ambient pressure X-ray photoelectron spectroscopy (APXPS) and a single-sided solid oxide electrochemical cell (SOC), we have studied the mechanism of electrocatalytic splitting of water ( $\text{H}_2\text{O} + 2\text{e}^- \rightarrow \text{H}_2 + \text{O}^{2-}$ ) and electro-oxidation of hydrogen ( $\text{H}_2 + \text{O}^{2-} \rightarrow \text{H}_2\text{O} + 2\text{e}^-$ ) at  $\sim 700^\circ\text{C}$  in 0.5 Torr of  $\text{H}_2/\text{H}_2\text{O}$  on ceria ( $\text{CeO}_{2-x}$ ) electrodes. The experiments reveal a transient build-up of surface intermediates ( $\text{OH}^-$  and  $\text{Ce}^{3+}$ ) and show the separation of charge at the gas–solid interface exclusively in the electrochemically active region of the SOC. During water electrolysis on ceria, the increase in surface potentials of the adsorbed  $\text{OH}^-$  and incorporated  $\text{O}^{2-}$  differ by 0.25 eV in the active regions. For hydrogen electro-oxidation on ceria, the surface concentrations of  $\text{OH}^-$  and  $\text{O}^{2-}$  shift significantly from their equilibrium values. These data suggest that the same charge transfer step ( $\text{H}_2\text{O} + \text{Ce}^{3+} \rightleftharpoons \text{Ce}^{4+} + \text{OH}^- + \text{H}^\bullet$ ) is rate limiting in both the forward (water electrolysis) and reverse ( $\text{H}_2$  electro-oxidation) reactions. This separation of potentials reflects an induced surface dipole layer on the ceria surface and represents the effective electrochemical double layer at a gas–solid interface. The in situ XPS data and DFT calculations show that the chemical origin of the  $\text{OH}^-/\text{O}^{2-}$  potential separation resides in the reduced polarization of the Ce–OH bond due to the increase of  $\text{Ce}^{3+}$  on the electrode surface. These results provide a graphical illustration of the electrochemically driven surface charge transfer processes under relevant and nonultrahigh vacuum conditions.



## INTRODUCTION

Understanding the mechanisms of charge separation and charge transfer at electrochemical interfaces is essential for the rational development of electrochemical devices, such as batteries, fuel cells, electrolyzers, and supercapacitors.<sup>1,2</sup> However, the materials and operating conditions employed in real world applications of these technologies are usually quite different from those used in surface science studies on model systems (i.e., the “pressure and materials gap”).<sup>3–5</sup> This disconnect is particularly problematic with high temperature electrochemical energy conversion devices with multicomponent materials (e.g., solid oxide fuel cells, electrolyzers, and electrocatalytic fuel processors)<sup>6</sup> for which in situ surface experiments at cell operating temperatures (typically  $>500^\circ\text{C}$ ) are challenging.<sup>7</sup> Because of the experimental constraints of most surface science experiments, the knowledge and understanding of the surface

processes at relevant conditions are limited and rely on extrapolations from ultrahigh vacuum (UHV) conditions and modeling studies.<sup>8</sup> As a result, the electrochemical surface processes are not well understood. For example, the non-Faradaic electrochemical modification of catalytic activity (NEMCA or EPOC)<sup>9</sup> can significantly enhance the rates of catalytic transformation of over 100 reactions,<sup>3,10</sup> yet the origins of this enhancement are not fully understood.<sup>3</sup> Even the mechanism of simple hydrogen electro-oxidation and water electrolysis on oxide surfaces of solid oxide electrochemical cells remains controversial with regard to the presence or absence of a double layer (dipole layer) at the gas–solid interface and the rate limiting processes on the oxide surfaces.<sup>11</sup>

Received: March 18, 2013

Published: July 3, 2013

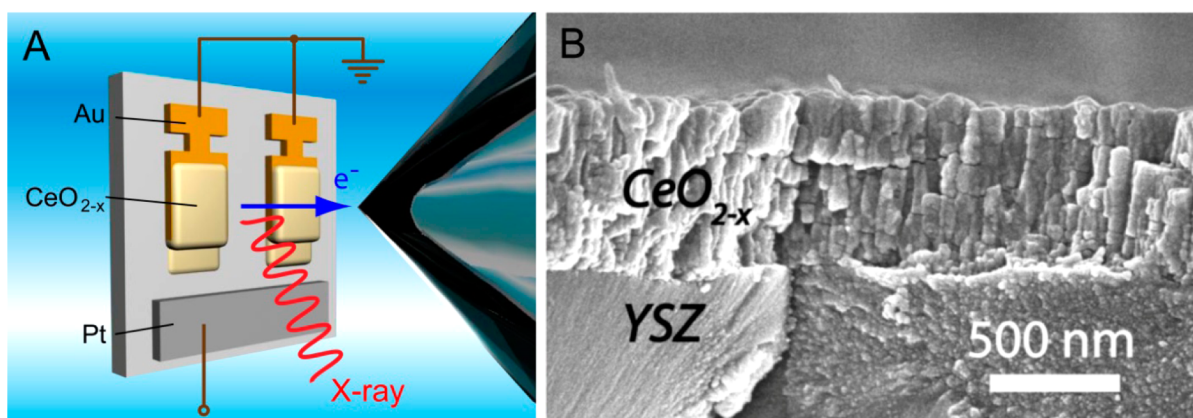


**Figure 1.** (A) Schematic drawing (not to scale) of the solid oxide electrochemical cell assembly. An alumina blocking layer is underneath the entire Au pad. (B) Cross-sectional scanning electron microscopy image showing the  $\sim 800$  nm ceria film deposited on the YSZ electrolyte of a fractured cell.

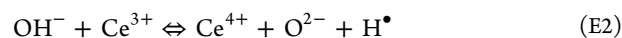
In previous publications, we showed how ambient pressure X-ray photoelectron spectroscopy can be used to monitor changes in Ce oxidation states in  $\text{CeO}_{2-x}$  electrodes, measure local surface potentials across an entire solid oxide electrochemical cell (SOC), and measure local overpotentials on operating SOC devices in far-from-equilibrium conditions.<sup>12,13</sup> These studies laid the groundwork for performing in situ mechanistic studies designed to “observe” charge separation at an SOC gas–solid interface and monitor changes in chemical intermediates involved in the electrochemical process. Our studies have focused on mixed ionic/electronic conductors (MIEC) such as ceria<sup>6,14,15</sup> because of their well-documented catalytic and electrocatalytic properties as well as their ability to extend the electrochemically active region beyond the three-phase boundary.<sup>12,13</sup> The catalytic behavior of ceria is directly linked to its accessible mixed valence  $\text{Ce}^{3+}/\text{Ce}^{4+}$  redox states, its oxygen storage capacity,<sup>6</sup> and surface vacancy concentrations.<sup>16</sup> Recent in situ studies on ceria and doped ceria have shown that surface oxygen vacancies are either linked to underlying  $\text{Ce}^{3+}$  ions or clustered around  $\text{Ce}^{3+}$  ions when vacancy concentrations are high.<sup>16,17</sup> While the oxygen mobility and catalytic behavior of ceria have been directly linked to the surface oxygen vacancy concentration,<sup>16</sup> the mechanisms of catalysis and electrocatalysis remain largely unknown.

In this study, we show that transient intermediates accumulate in the active region of a ceria SOC as a result of rate-limiting charge transfer processes. The same electrochemical step,  $\text{H}_2\text{O} + \text{Ce}^{3+} \rightleftharpoons \text{Ce}^{4+} + \text{OH}^- + \text{H}^\bullet$ , appears to be rate limiting in both the forward (water electrolysis) and reverse ( $\text{H}_2$  electro-oxidation) reactions. The mechanistic insight was obtained from monitoring the build-up of  $\text{Ce}^{3+}$  and  $\text{OH}^-$  at positive and negative biases, respectively. In addition, we observe a separation of local surface potentials of the adsorbed  $\text{OH}^-$  and incorporated  $\text{O}^{2-}$  ions due to a build-up of surface  $\text{Ce}^{3+}$ . The in situ XPS<sup>18</sup> data and DFT calculations show that the chemical origin of the  $\text{OH}^-/\text{O}^{2-}$  potential separation resides in the reduced polarization of the Ce–OH bond due to the  $\text{Ce}^{3+}$  buildup. This charge separation can be viewed as the effective double layer at an electrochemical gas–solid interface<sup>10,19</sup> and is interpreted in the context of Fleig’s description of surface potential steps on MIEC electrodes.<sup>19</sup> These results provide insight into the high temperature surface chemistry on mixed ionic/electronic conducting ceria ( $\text{CeO}_{2-x}$ ) electrodes.<sup>15,20–23</sup>

## RESULTS AND DISCUSSION

The single-chamber polycrystalline yttria-stabilized zirconia (YSZ) cell consists of a Pt counter electrode and ceria working electrodes with Au current collectors (Figure 1A). Dense thin ceria films were sputtered on top of Au films with elongated Au pads exposed for electrical connections. Underneath the Au films, 30 nm thick alumina films were sputtered to block the  $\text{O}^{2-}$  transport between YSZ and Au. Only one ceria edge has direct contact with the YSZ electrolyte, which defines the current flow region. The outer ceria edge is  $\sim 300$   $\mu\text{m}$  from the nearest Pt electrode edge. In situ APXPS and electrochemical studies were conducted at  $\sim 700$   $^\circ\text{C}$  with 0.5 Torr of 1:1  $\text{H}_2/\text{H}_2\text{O}$  mixtures. An overview of the cell fabrication process is described in the Experimental Section, and a detailed description can be found in ref 13.

At open circuit voltage (OCV), the ceria surface is at thermal equilibrium with the  $\text{H}_2$  and  $\text{H}_2\text{O}$  gases as described by the following four basic exchange equilibria:



These four exchange reactions represent the interactions between  $\text{H}_2\text{O}$  and  $\text{OH}^-$  (E1),  $\text{OH}^-$  and  $\text{O}^{2-}$  (E2), and surface hydrogen atoms  $\text{H}^\bullet$  and  $\text{H}_2$  (E3) and electron transport by way of polaron hopping (E4). Since there is no net current flow in the cell at OCV, the surface cerium redox states and the surface hydroxyl coverage adopt equilibrium concentrations dictated by the cell temperature and gas partial pressures. However, when a bias is applied between the counter electrode (Pt) and working electrode ( $\text{CeO}_{2-x}$ ), current flows through the cell and these reactions can be shifted from their equilibrium positions. For example, when Pt is positively biased relative to ceria,  $\text{O}^{2-}$  ions are driven from the surface of ceria down to the YSZ electrolyte and out to the Pt electrode while electrons move from the gold current collector to the ceria surface. Under these conditions, the forward reactions E1–E4 are favored on ceria, which results in water electrolysis, whereas hydrogen electro-oxidation is promoted on the Pt electrode. The water electrolysis process on ceria is illustrated in Figure 2. When the bias is reversed

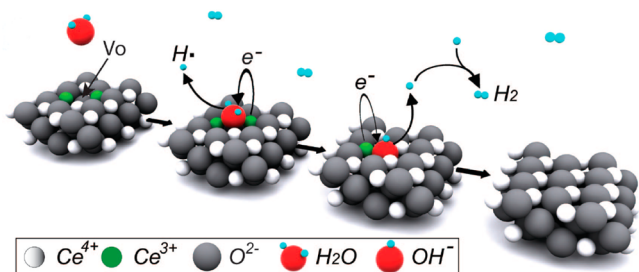


**Figure 2.** Proposed surface electrochemical reaction mechanism under positive applied bias. Water-splitting reactions occur on ceria electrodes.  $V_O$  is an oxide vacancy on the ceria surface. For clarity, the surface H atoms ( $H^*$ ) are drawn above the electrode surface.

(negative bias on Pt), the surface reactions are shifted in the opposite direction to give hydrogen electro-oxidation on ceria and water electrolysis at Pt. The current-induced equilibrium shifts only occur in the electrochemically active regions, namely, the Pt-YSZ three-phase boundary and the  $\sim 400 \mu\text{m}$  region of ceria covering the Au-YSZ interfacial edge.<sup>12</sup> The electrochemically active regions on ceria are defined by large surface potential drops and shifts in the equilibrium  $\text{Ce}^{3+}/\text{Ce}^{4+}$  ratios.<sup>12</sup> In the inactive regions of the ceria electrode, the absence of a net current leaves the ceria redox states and hydroxyl adsorbate concentrations in their equilibrium conditions regardless of the applied potential.

The surface bias and surface concentrations of  $\text{OH}^-$  and  $\text{O}^{2-}$  on an 800 nm thick ceria electrode were determined through in situ measurements of the O 1s XPS spectra (Figure 3). Two-dimensional (2D) APXPS spectral maps (binding energy (BE) versus position) were constructed by using the differentially pumped electron analyzer installed on beamline 9.3.2 at the Advance Light Source in Berkeley.<sup>24,25</sup> Figure 3A shows the second derivative of 2D O 1s XPS intensity spectral maps in the active regions of ceria electrode at +1.2 V applied bias. The three peaks are due to  $\text{O}^{2-}$  ions in the ceria electrode ( $\sim 528 \text{ eV}$ ), the surface  $\text{OH}^-$  ( $\sim 529.7 \text{ eV}$ ),<sup>26</sup> and gas phase water ( $533.8 \text{ eV}$ ) near the electrode.<sup>27</sup> To clearly illustrate the bias-induced peak shifts of O 1s spectra, the second derivatives of 2D O 1s XPS intensity spectral maps are plotted in the active regions of ceria electrode. Depth profile studies of the O 1s spectra (Figure S1) confirm that the  $\text{OH}^-$  species (BE  $\approx 529.7 \text{ eV}$ ) are on the surface of the ceria electrode while the  $\text{O}^{2-}$  signal represents an average of the oxide ions in the solid phase very near the surface (see Experimental Section). The spatially resolved individual XPS spectra can be obtained by taking one-dimensional slices from the 2D intensity spectral maps. The peak fitting of a typical O 1s spectrum is shown in Figure 3B.

We have previously shown that the apparent binding energy of an electron in a surface atom at an applied bias ( $\text{BE}_{\text{Bias}}$ ) is a direct measure of the local surface potential of that atom ( $V_L$ ) when compared to its binding energy at OCV, where  $V_L = \text{BE}_{\text{Bias}} - \text{BE}_{\text{OCV}}$ .<sup>12,28–30</sup> As such, the 2D XPS data collected at

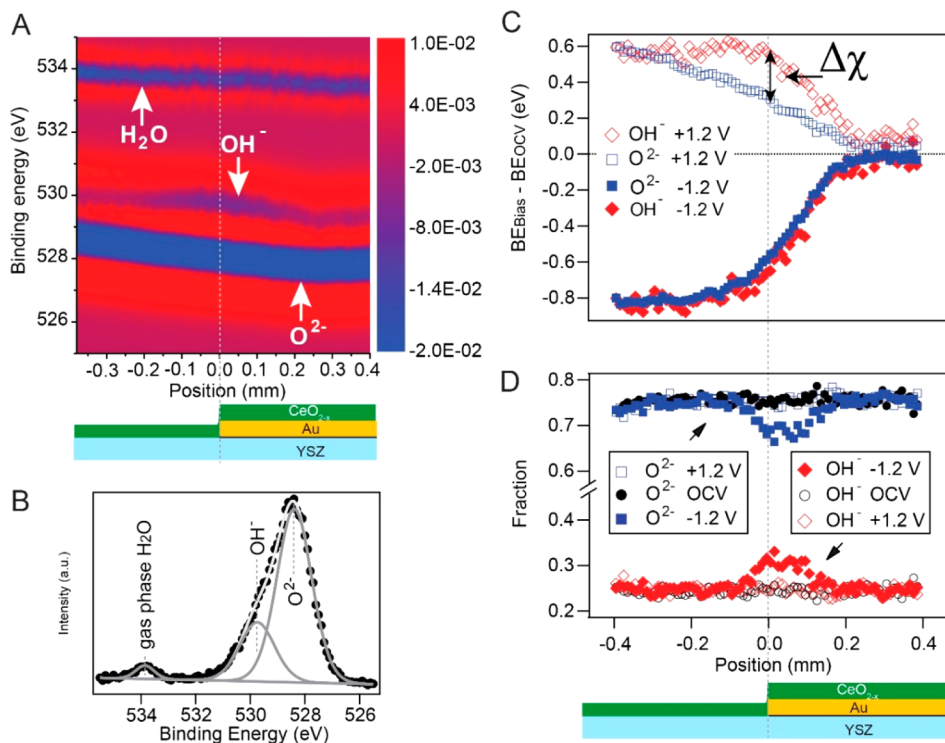


**Figure 3.** Spatially resolved O 1s XPS spectra detected on a 800 nm thick ceria electrode under conditions of  $\sim 700^\circ\text{C}$ , 0.5 Torr of 1:1  $\text{H}_2/\text{H}_2\text{O}$  mixture. The cell was tested in three electrochemical conditions including  $\pm 1.2 \text{ V}$  applied biases and the open circuit voltage (OCV), i.e., the equilibrium condition without an applied bias. (A) Spatially resolved second derivative of the two-dimensional O 1s spectra that was collected under +1.2 V applied bias. The horizontal axis is the position on the cell surface. A schematic drawing of the cell is shown and aligned to position. The alumina blocking layer is denoted by the black line between the Au pad and the YSZ electrolytes. The cell position (mm) is determined by carefully examining the distance between Pt and Au edges in the cell photos, and the Pt edge is determined by the disappearance of Pt and appearance of Zr in XPS. (B) One slice of O 1s spectra at  $x = -0.155 \text{ mm}$  under +1.2 V, fitted with gas-phase water, hydroxyl surface adsorbates, and solid-phase oxide. (C) Relative shifts in apparent binding energy under applied bias away from OCV for  $\text{OH}^-$  and  $\text{O}^{2-}$  peaks. The local potential difference between  $\text{OH}^-$  and  $\text{O}^{2-}$  represents the difference of surface potential steps ( $\Delta\chi$ ). (D) Fraction of  $\text{OH}^-$  and  $\text{O}^{2-}$  under OCV and  $\pm 1.2 \text{ V}$  applied biases.

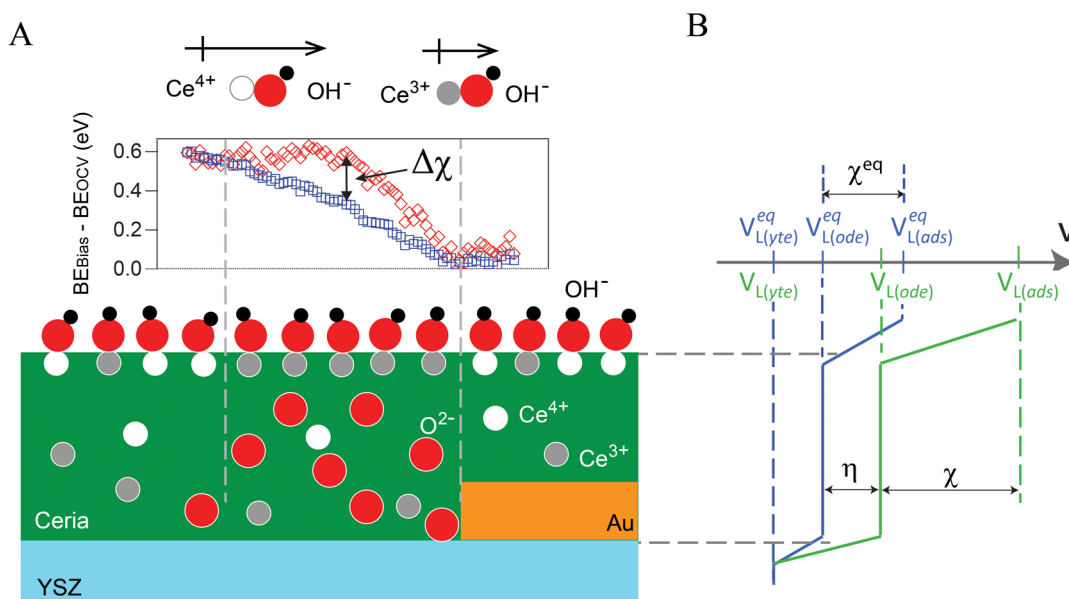


**Figure 4.** (A) Schematic representation of relative bond polarities (bond dipoles) for the  $\text{Ce}^{3+}$ -OH and  $\text{Ce}^{4+}$ -OH interactions on the ceria surface. The electrochemically induced build-up in  $\text{Ce}^{3+}$  concentration results in a divergence in the local surface potentials of OH<sup>-</sup> (red) and O<sup>2-</sup> (blue) within the active region denoted by the dashed lines in (A). (B) Interpretation of the potential losses across the gas-solid interface and ceria-YSZ interface showing the surface potential steps ( $\chi$ ) and the charge transfer overpotential ( $\eta$ ). The schematic is a modified version of Fleig's model.<sup>19</sup> In the scheme above, the local equilibrium potentials of the YSZ electrolyte, the ceria electrode, and hydroxyl adsorbate layers are shown in blue and are labeled  $V_{L(\text{yte})}^{\text{eq}}$ ,  $V_{L(\text{ode})}^{\text{eq}}$ ,  $V_{L(\text{ads})}^{\text{eq}}$ , respectively. The local potentials observed at an applied cell bias of +1.2 V are shown in green and denoted by  $V_{L(\text{yte})}$ ,  $V_{L(\text{ode})}$ ,  $V_{L(\text{ads})}$ , respectively. For simplicity, all of the local potentials are normalized to the equilibrium YSZ electrolyte potential. In our single-sided half cell, all equilibrium cell potentials are equal to 0.0 V. See text for definitions.

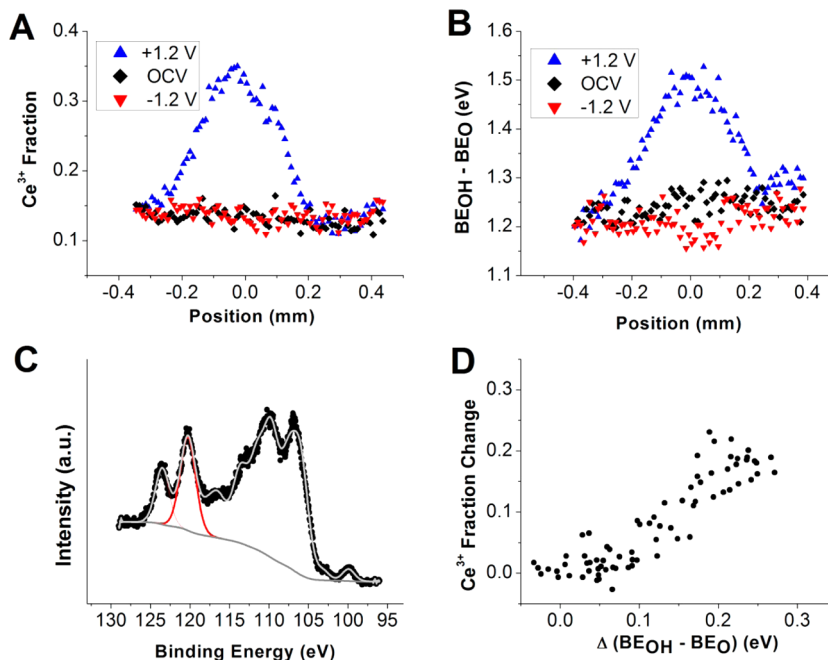


**Figure 5.** (A) Spatially resolved cerium redox changes ( $\text{Ce}^{3+}$  fraction) calculated from fitted Ce 4d spectra under OCV and  $\pm 1.2$  V applied biases. (B) Spatially resolved binding energy separations (i.e., surface potential steps) between surface adsorbates (OH<sup>-</sup>) and solid surface (O<sup>2-</sup>) derived from O 1s spectra under OCV and  $\pm 1.2$  V applied biases. (C) Example of Ce 4d peak fitting. (D) Correlation between  $\text{Ce}^{3+}$  fraction changes and surface potential step changes under +1.2 V applied bias versus OCV. The  $\text{Ce}^{3+}$  positions were corrected for a 50  $\mu\text{m}$  experimental shift associated with using different beam energies in different XPS measurements.

an applied bias provide a map of the spatially resolved local surface potentials of all atoms on the SOC surface. In Figure 3C, we show how the local surface potential of OH<sup>-</sup> and O<sup>2-</sup> shift under applied biases across the active region of the ceria electrode. Across the surface of the SOC, the  $V_L$  values for all of

the surface species (i.e., OH<sup>-</sup>, O<sup>2-</sup>,  $\text{Ce}^{3+}$ ,  $\text{Zr}^{4+}$ ) shift by the same amount<sup>13</sup> provided that they are outside of the electrochemically active region of the ceria electrode. However, when water-splitting reactions are favored on ceria (positive bias), the  $V_L$  values for OH<sup>-</sup> and O<sup>2-</sup> are significantly different

in the active regions of the ceria (Figure 3C). Under these conditions, the  $\text{Ce}^{3+}/\text{Ce}^{4+}$  ratios are also driven away from equilibrium, showing a large increase in surface  $\text{Ce}^{3+}$  concentration in the same region (Ce 4d XPS spectra, Figure 5A). Outside the active region, the  $V_L$  values for  $\text{OH}^-$  and  $\text{O}^{2-}$  once again become equivalent and the  $\text{Ce}^{3+}/\text{Ce}^{4+}$  ratios maintain their equilibrium values. This difference in the local surface potentials of  $\text{OH}^-$  and  $\text{O}^{2-}$  ( $V_{L(\text{OH}^-)} - V_{L(\text{O}^{2-})}$ ) in the active region represents the local potential difference between the surface adsorbates and the ceria electrode. The build-up of surface  $\text{Ce}^{3+}$  in the active region drives the separation of the potentials (vide infra). When  $\text{H}_2$  electro-oxidation is promoted on ceria (negative bias), the  $V_L$  values for  $\text{OH}^-$  and  $\text{O}^{2-}$  show a very small but discernible divergence but in the opposite direction (Figures 3C and 5B). The origins of the divergent  $V_L$  values are described below.

The dipole model<sup>31–33</sup> at gas–solid interfaces<sup>34,35</sup> can illustrate the divergence of the  $\text{OH}^-$  and  $\text{O}^{2-}$  surface potentials in the active regions of the SOC. The chemisorbed  $\text{OH}^-$  ions are bonded to ceria on the SOC surface with natural bond dipoles, with the negative end pointing to  $\text{OH}^-$  oxygen and the positive end to the  $\text{Ce}^{3+}/\text{Ce}^{4+}$  ions. Reactions E1 and E2 shift the concentrations of charged surface species on either side of the dipole layer and, therefore, modify the magnitude of the surface dipole. At +1.2 V applied bias, the  $\text{OH}^-/\text{O}^{2-}$  concentration ratio shows no change in the active region relative to the equilibrium conditions at OCV (Figure 3D). However, the large increase of surface  $\text{Ce}^{3+}$  ions (i.e., polarons) in the active region (Figure 5A) significantly reduces the magnitude of the dipole moment between the surface  $\text{OH}^-$  adsorbate and the electrode. The buildup of  $\text{Ce}^{3+}$  ions and associated surface vacancies reduces the Ce–OH bond polarization relative to  $\text{Ce}^{4+}$  dominated surface. This electrochemically driven reduction in bond polarization effectively decreases the local surface potentials on the two sides of the dipole layer. Specifically, the hydroxyl adsorbate,  $V_{L(\text{OH}^-)}$ , is driven to a higher local potential than that of the ceria electrode surface directly beneath it (i.e., the oxide potential,  $V_{L(\text{O}^{2-})}$ , Figure 3C). Consequently, the BE difference between hydroxyl adsorbates and electrode oxides becomes larger than that of the OCV condition in the active region (Figure 5B). The correlation of surface  $\text{Ce}^{3+}$  buildup with divergence of  $V_{L(\text{OH}^-)}$  and  $V_{L(\text{O}^{2-})}$  values (Figure 5D) further confirms the origin of this potential separation.

The situation is substantially different at –1.2 V applied bias ( $\text{H}_2$  electro-oxidation on ceria). Under these conditions, the ceria surface shows little change in  $\text{Ce}^{3+}/\text{Ce}^{4+}$  ratios (Figure 5A), yet there is a small but significant increase in the  $\text{OH}^-$  adsorbate concentration in the active region with an accompanying decrease in surface  $\text{O}^{2-}$  concentration (Figure 3D).

To elucidate the interplay between surface structure and mechanisms of charge transfer processes at electrochemical interfaces of the ceria electrode, O 1s core level of  $\text{OH}^-$  and  $\text{O}^{2-}$  on ceria (111) surface were calculated using spin-polarized total energy calculations, as implemented in the Vienna Ab Initio Simulation Package (VASP), version 5.2.<sup>36–40</sup> Though the accurate calculation of the absolute value of the core level remains indeterminable, the relative difference, i.e., the so-called core-level shift (CLS), between different species of interest can be well described.<sup>41–43</sup> For O 1s considered in the present work the calculated sequence of O 1s (gas  $\text{H}_2\text{O}$ ) > O 1s ( $\text{OH}^-$ )

> O 1s ( $\text{O}^{2-}$ ) (Figure S2) indeed agrees well with the experimental results shown in Figure 3B.

The O 1s core level XPS shifts of the surface  $\text{OH}^-$  and  $\text{O}^{2-}$  show a strong correlation to the calculated DFT CLS of the  $\text{OH}^-$  and  $\text{O}^{2-}$  species under simulated conditions. To compare the O 1s CLSs measured at different experimental conditions, we calculated  $\text{OH}^-$  CLSs using models containing different types of oxygen vacancies and different oxygen vacancy coverage. We found that the difference between  $\text{OH}^-$  and  $\text{O}^{2-}$  in O 1s CLSs increases by 0.3 eV as the  $\text{O}^{2-}$  vacancy coverage increases from  $1/16$  to  $3/16$  ML. The difference also increases by 0.50 eV when a single  $\text{O}^{2-}$  vacancy is replaced by a dimer oxygen vacancy (one surface vacancy and one subsurface vacancy). Both of these two scenarios agree well with the observation that the BE difference of  $\text{OH}^-$  and  $\text{O}^{2-}$  reaches 0.25 eV under +1.2 V applied bias (Figure 3C), where the ceria surface is more reduced. However, the separation between  $\text{OH}^-$  and  $\text{O}^{2-}$  in O 1s CLSs decreases by 0.3 eV when a single oxygen vacancy is replaced by a linear surface oxygen vacancy cluster (LSVC).<sup>16,20</sup> These findings lead us to believe that vacancy clusters are not formed on the ceria electrode surface under +1.2 V applied bias but rather isolated surface vacancies linked with surface  $\text{Ce}^{3+}$  occur under these conditions, as previously observed in other systems.<sup>16</sup> In contrast, the value of calculated  $\text{OH}^-$  O 1s CLS (~2.7 eV) does not change significantly when the  $\text{OH}^-$  coverage increases from  $1/16$  to  $3/16$  for a given vacancy coverage. This finding agrees well with the measured local potentials under –1.2 V applied bias (Figure 3C), where no significant difference in local potentials between  $\text{OH}^-$  and  $\text{O}^{2-}$  is detected. The observed 0.25 V separation of  $\text{OH}^-$  and  $\text{O}^{2-}$  surface potentials and the calculated 0.3 eV increases in the CLSs at +1.2 V are also in agreement with the experimental studies of Mullins et al. who showed that there is a 0.3 eV shift of the  $\text{O}^{2-}$  BEs to higher energy for  $\text{Ce}^{3+}$  oxide relative to  $\text{Ce}^{4+}$  oxide.<sup>26</sup>

$\text{Ce}^{3+}$  and  $\text{OH}^-$  are both surface intermediates in the ceria-catalyzed electro-oxidation of  $\text{H}_2$  and  $\text{H}_2\text{O}$  electrolysis processes. Shifts in their concentrations provide insight into rate-limiting surface processes. At –1.2 V, the accumulation of  $\text{OH}^-$  adsorbates in the active region indicates that  $\text{OH}^-$  consumption is rate-limiting, i.e., the reverse reaction of E1. At +1.2 V, the  $\text{OH}^-$  maintains its equilibrium concentration while the  $\text{Ce}^{3+}$  concentration increases significantly. The buildup of surface  $\text{Ce}^{3+}$  and the lack of changes in  $\text{OH}^-/\text{O}^{2-}$  concentration ratio are also consistent with E1 being a rate-limiting process. As such, our results suggest that the first step in water electrolysis ( $\text{H}_2\text{O} + \text{Ce}^{3+} \rightarrow \text{Ce}^{4+} + \text{OH}^- + \text{H}^*$ ) and the last step in hydrogen electro-oxidation ( $\text{Ce}^{4+} + \text{OH}^- + \text{H} \rightarrow \text{H}_2\text{O} + \text{Ce}^{3+}$ ) are rate-limiting steps on the ceria-based SOC electrocatalysts described here. Increases in  $\text{OH}^-$  concentrations have also been observed in a related study<sup>44</sup> on YSZ electrolyte surfaces near the three-phase boundary regions in polarized Pt-YSZ-Pt symmetrical electrolysis cells.

The data here can also be described by the Fleig model<sup>19</sup> for SOC surface reactions associated with MIEC materials such as ceria (Figure 4B). The model highlights the differences between liquid–solid electrochemical interfaces described by classical Butler–Volmer kinetics and gas–solid electrochemical interfaces where double layers involve reactant species. Central to this model is the existence of equilibrium surface potential step ( $\chi^{\text{eq}}$ ) describing the effective resistance to charge separation of reaction intermediates at a metal oxide electrode surface (e.g.,  $\text{OH}^- + \text{Ce}^{3+} \rightarrow \text{Ce}^{4+} + \text{O}^{2-} + \text{H}^*$ ). Physically, this

resistance is equal to the difference between the local surface potentials of the adsorbates and the electrode under equilibrium conditions, described as the equilibrium surface potential step:

$$\chi^{\text{eq}} = V_{L(\text{ode})}^{\text{eq}} - V_{L(\text{ads})}^{\text{eq}}$$

When the electrode is biased, a modified surface potential step is obtained ( $\chi$ ) that represents a shift from equilibrium conditions (Figure 4B). The new  $\chi$  is equal to the potential difference between the surface adsorbates and the electrode under applied bias ( $\chi = V_{L(\text{ode})} - V_{L(\text{ads})} = V_{L(\text{O})} - V_{L(\text{OH})}$ ). The difference between the equilibrium potential step and the potential step at bias is defined as  $\Delta\chi = \chi - \chi^{\text{eq}}$ . This shift in surface potential step drives the net electrochemical reactions and generates current.<sup>19</sup>  $\Delta\chi$  is also a direct measure of the electrochemical double layer at the gas–solid interface.<sup>19</sup>

The measurements of the divergent  $V_L$  values for the  $\text{OH}^-$  and  $\text{O}^{2-}$  at +1.2 V represent the potential drop between the adsorbate ( $V_{L(\text{OH})}$ ) and the underlying ceria surface ( $V_{L(\text{O})}$ ) and thus a direct measure of  $\Delta\chi = V_{L(\text{OH})} - V_{L(\text{O})}$ . In a traditional fuel cell, such as that described by Fleig (Figure 4B), there is a finite equilibrium potential step ( $\chi^{\text{eq}}$ ) that describes the inherent resistance to surface charge separation resulting from the electrochemical potential of the cell. In our case, all equilibrium potentials are zero because OCV is 0.0 V in a single sided cell, and as a result,  $\Delta\chi = \chi$  in our experiments. The value of  $\Delta\chi$  reaches a maximum of 0.25 V in the center of the active region (Figure 4A). The correlation between surface  $\text{Ce}^{3+}$  concentrations and the magnitudes of  $\Delta\chi$  (Figure 5D) confirms that this surface potential step is related to the relative rates of oxygen supply and removal at the surface.

The surface potential steps are different from activation overpotentials ( $\eta$ ) associated with charge transfer reactions at phase boundaries. Overpotentials describe barriers to net charge transfer across a double layer,<sup>45,46</sup> whereas there is no net charge transfer associated with surface potential steps across the gas–solid interface. However, the changes in bond polarities and the resulting dipoles between surface adsorbates and the electrode surface form an effective double layer at the gas–solid interface, which modifies surface reactions involving charged species. The inherent coupling of reaction intermediate concentration shifts (i.e.,  $\text{OH}^-$  and  $\text{Ce}^{3+}$ ) and surface potential steps must be included in an accurate kinetic description of gas–solid interfacial reactions involving charge exchange with the underlying surface, as described in Fleig's model.<sup>19</sup> For high-temperature SOC systems, in situ surface studies are the only means of extracting such information, and the results described herein provide a significant advance in these endeavors.

## CONCLUSION

These experiments provide a picture of charge separation at a gas–solid interface of a working electrochemical device. Similar to electrical double layers between the electrode and the electrolyte, this charge separation leads to an enormous electric field ( $\sim 10^8$  V/m) within a small interface region that greatly affects surface reaction kinetics in electrochemically active materials and in particular oxides. The interplay between this enormous electric field and the chemical reactions at the interface is, in a sense, the essence of high-temperature solid–gas electrochemistry.<sup>47</sup>

## EXPERIMENTAL SECTION

**Solid Oxide Electrochemical Cell Preparation and Characterization.** Detailed descriptions of cell fabrication and characterization methods can be found in ref 13. A brief overview is given here. YSZ powder was purchased from Tosoh Inc. The powder was pressed and cut into square pellets. After firing at 1450 °C for 3 h, the final dimensions of the pellets were 10 mm  $\times$  10 mm  $\times$  1 mm. Patterned  $\text{Al}_2\text{O}_3$ , Au, and Pt electrodes were sputter-deposited using an AJA International, ATC 1800 V sputtering unit. The thicknesses of the sputtered  $\text{Al}_2\text{O}_3$ , Au, and Pt films are 30, 300, and 300 nm, respectively.  $\text{CeO}_2$  films were sputter-deposited using a Lesker PVD 75 sputter unit under 5 mTorr of  $\text{O}_2/\text{Ar}$  gas mixture containing 10%  $\text{O}_2$ . Samples were annealed at 800 °C for 3 h prior to XPS or electrochemistry testing. Postprocessing SEM analysis was conducted on a Hitachi SU-70 analytical ultrahigh resolution scanning electron microscope.

**Electrochemical Characterization.** Electrochemical measurements were collected simultaneously with XPS data at beamlines 9.3.2 and 11.02 of Advanced Light Source, Lawrence Berkeley National Laboratory. The lateral spatial resolution of the area detector at beamline 9.3.2 is 16–20  $\mu\text{m}$ . Detailed descriptions of the electrochemical setup can be found in ref 13. Briefly, a Bio-Logic potentiostat was used for two-probe linear sweep voltammetry (LSV) and electrochemical impedance spectroscopy (EIS) characterizations. Since the working electrode (Au pad) was grounded to the XPS chamber, the cell bias is defined as the potential difference between the Pt counter electrode and the Au current collector;  $V_{\text{Cell}} \equiv V_{\text{Pt}} - V_{\text{Au}}$ . Results of electrochemical measurements are shown in Figure S3. The grounded working electrode allows for the direct measure of local surface potential by monitoring shifts in apparent binding energies versus the OCV values. As such, the XPS shifts in surface binding energy are referenced against a grounded Au pad and represent measures of ohmic loss versus a contact-free reference electrode at every point in the cell. The quantitative analyses of surface potentials and interfacial overpotentials by this method have been described in refs 12 and 13.

**1s Binding Energies of  $\text{OH}^-$ ,  $\text{O}^{2-}$ , and Gas Phase  $\text{H}_2\text{O}$ .** The BE of O 1s presented here is referenced to the valence band maximum, which is  $\sim 2$  eV below the Fermi level. Since we are only interested in the relative shifts between different O 1s peaks, the absolute BE values of different O 1s peak positions are not important in this study. In general, the O 1s BEs of  $\text{OH}^-$ ,  $\text{O}^{2-}$ , and gas phase  $\text{H}_2\text{O}$  here are 2 eV less than the BE values found in previous literature, which are typically referenced to the Fermi level.

**$\text{OH}^-$  Surface Species.** To confirm that assigned  $\text{OH}^-$  species are surface species, we performed depth profiling using variable energy incident X-rays at ALS beamline 11.0.2.<sup>48</sup> The O 1s spectra were collected at photon energies of 690, 840, 1140, and 1320 eV under similar conditions. The photoelectron kinetic energies of the O 1s region are  $\sim 160, 310, 610,$  and 790 eV, respectively. Since the inelastic mean free path (IMFP) of a photoelectron increases with kinetic energy in the energy range of these experiments, decreasing the photon energy causes the spectra to be more surface sensitive and increasingly reflective of the topmost surface layer. The spectra in Figure S1 have a Shirley background subtracted and are fitted with a symmetric Voigt profile. As the photon energy increases from 690 to 1320 eV, the relative area of the  $\text{OH}^-$  peak decreases with respect to the bulk  $\text{O}^{2-}$  peak while that of the water gas phase peak decreases as well. The relative decreases in  $\text{OH}^-$  and gas phase water peak with respect to  $\text{O}^{2-}$  with increasing photon energy are expected, since these atoms are only found in the surface layer and gas phase molecules are in fixed concentration above the sample surface.

**Determination of the Inelastic Mean Free Path (IMFP).** The IMFP was calculated using the NIST Standard Reference Database 71 “NIST Electron Inelastic-Mean-Free-Path Database”, version 1.1.<sup>49</sup> The software program provides the ability to predict the IMFP for inorganic compounds supplying the stoichiometric composition of  $\text{CeO}_2$ . For incident photon beam energies ranging from 690 to 1320 eV the IMFP was estimated to be 0.65–1.67 nm, respectively.

**Estimating the Electric Field at the Dipole Layer.** To semiquantitatively estimate the separation between OH<sup>-</sup> and the O<sup>2-</sup> surface ions, we used a simple two-layer model to estimate the order of magnitude of such a separation. Assuming an overlayer of Ce(OH)<sub>x</sub> on top of CeO<sub>2</sub> bulk, the thickness of such an overlayer,  $d_{ov}$ , can be estimated using

$$\frac{d_{ov}}{\cos \alpha} = d = \lambda \ln \left( \frac{n_{sub} R_{ov} + 1}{n_{ov}} \right)$$

where  $d$  is the distance the photoelectron traveled across the overlayer and  $\alpha$  is the emission angle of electrons relative to the surface normal ( $\alpha$  is equal to 40° and 0° at beamlines 11.0.2 and 9.3.2, respectively),  $R_{ov}$  is the intensity ratio of  $I(\text{OH}^-)$  and  $I(\text{O}^{2-})$ ,  $n_{ov}$  and  $n_{sub}$  are the densities of the overlayer and substrate, and  $\lambda$  is the IMFP of photoelectrons.

Several assumptions have been made: the overlayer has a constant thickness; there is a sharp boundary between the overlayer and the substrate; the overlayer and the substrate have the same IMFP for a given photon energy. Furthermore, we assume  $(n_{sub})/(n_{ov}) = 1$ . We can fit our data with the formula above. We find that  $d = 1$  nm gives the best fit (Figure 5D), which leads to a  $d_{ov}$  of 0.8 nm. This will give an average separation of 0.4 nm. This oversimplified model is only used here to estimate the order of magnitude of charge separation. The field strength change then can be estimated to be about  $(0.25 \text{ V})/(0.4 \text{ nm}) \approx 10^8 \text{ V/m}$ .

**Correlation of Surface Ce<sup>3+</sup> Fractions and the Surface Dipole.** Under +1.2 V applied bias, the surface cerium oxidation states are largely driven away from equilibrium that leads to a higher Ce<sup>3+</sup> concentration in the active region (Figure 5A). There is a striking similarity between the dipole strength change across the cell and Ce<sup>3+</sup> concentration change. Our data (Figure 5D) show a strong linear correlation between the changes in Ce<sup>3+</sup> concentration (Figure 5A) and changes in OH<sup>-</sup> BE shift (Figure 5B).

**Theoretical Approaches and Computational Details.** Spin-polarized total energy calculations were performed based on the all-electron projected augmented wave (PAW) method and DFT + U method within the generalized gradient approximation (GGA-PW91) functional as implemented in the Vienna Ab Initio Simulation Package (VASP), version 5.2.<sup>36–38</sup> A cutoff of 400 eV was used for the plane wave expansion. The value of the  $U$  is set to 5 eV, as used in previous calculations.<sup>39,40</sup> A CeO<sub>2</sub>(111)-p(4×4) slab with three CeO<sub>2</sub> layer thickness separated by 15 Å vacuum was used to model the ceria surfaces with different coverage of oxygen vacancy and hydroxyl, and only  $\Gamma$ -points were used to sample the surface Brillouin zone. All atoms in the super cell were relaxed until the residual force on each atom was less than 0.01 eV Å<sup>-1</sup>. For the core level shift calculations including the final state effect, an electron is removed from the core by generating the corresponding core excited ionic PAW potential in the course of the calculation and remaining core states are relaxed along the self-consistent calculation.<sup>41–43</sup>

## ■ ASSOCIATED CONTENT

### Supporting Information

XPS depth profile for O 1s spectra (Figure S1), schematic representations of CLSs calculations (Figure S2), and electrochemical characterizations of LSV and EIS (Figure S3). This material is available free of charge via the Internet at <http://pubs.acs.org>.

## ■ AUTHOR INFORMATION

### Corresponding Author

\*zliu2@lbl.gov; eichhorn@umd.edu

### Author Contributions

<sup>#</sup>C.Z., Y.Y., and M.E.G. are equal contributors.

### Notes

The authors declare no competing financial interest.

## ■ ACKNOWLEDGMENTS

This work was funded by the ONR through Contract N000141110121. The Advanced Light Source is supported by the Director, Office of Science, Office of Basic Energy Sciences, of the U.S. Department of Energy under Contract DE-AC02-05CH11231. We thank the University of Maryland Nanocenter and the University of Maryland Energy Research Center (UMERC) and the National Natural Science Foundation of China (Grants 21173210, 21225315) for support.

## ■ REFERENCES

- (1) Bard, A. J. *Electrochemical Methods: Fundamentals and Applications*, 2nd ed.; Wiley: New York, 2001.
- (2) Greiner, M. T.; Helander, M. G.; Tang, W.-M.; Wang, Z.-B.; Qiu, J.; Lu, Z.-H. *Nat. Mater.* **2011**, *11*, 76–81.
- (3) Imbihl, R. *Prog. Surf. Sci.* **2010**, *85*, 241–278.
- (4) Somorjai, G. A.; Park, J. Y. *Chem. Soc. Rev.* **2008**, *37*, 2155.
- (5) Diebold, U. *Surf. Sci. Rep.* **2003**, *48*, 53–229.
- (6) Sun, C.; Li, H.; Chen, L. *Energy Environ. Sci.* **2012**, *5*, 8475.
- (7) Mutoro, E.; Crumlin, E. J.; Pöpke, H.; Luerssen, B.; Amati, M.; Abyaneh, M. K.; Biegalski, M. D.; Christen, H. M.; Gregoratti, L.; Janek, J.; Shao-Horn, Y. J. *Phys. Chem. Lett.* **2012**, *3*, 40–44.
- (8) Ganduglia-Pirovano, M. V.; Hofmann, A.; Sauer, J. *Surf. Sci. Rep.* **2007**, *62*, 219–270.
- (9) Vayenas, C. G.; Koutsodontis, C. G. *J. Chem. Phys.* **2008**, *128*, 182506.
- (10) Vayenas, C. G.; et al. *Electrochemical Activation of Catalysis: Promotion, Electrochemical Promotion, and Metal–Support Interactions*; Kluwer Academic/Plenum Publishers: New York, 2001.
- (11) Zhu, H.; Kee, R. J.; Janardhanan, V. M.; Deutschmann, O.; Goodwin, D. G. *J. Electrochem. Soc.* **2005**, *152*, A2427.
- (12) Zhang, C.; Grass, M. E.; McDaniel, A. H.; DeCaluwe, S. C.; Gabaly, F. E.; Liu, Z.; McCarty, K. F.; Farrow, R. L.; Linne, M. A.; Hussain, Z.; Jackson, G. S.; Bluhm, H.; Eichhorn, B. W. *Nat. Mater.* **2010**, *9*, 944–949.
- (13) Zhang, C.; Grass, M. E.; Yu, Y.; Gaskell, K. J.; DeCaluwe, S. C.; Chang, R.; Jackson, G. S.; Hussain, Z.; Bluhm, H.; Eichhorn, B. W.; Liu, Z. *ACS Catal.* **2012**, *2*, 2297–2304.
- (14) Kharton, V. V.; Figueiredo, F. M.; Navarro, L.; Naumovich, E. N.; Kovalevsky, A. V.; Yaremchenko, A. A.; Viskup, A. P.; Carneiro, A.; Marques, F. M. B.; Frade, J. R. J. *Mater. Sci.* **2001**, *36*, 1105–1117.
- (15) *Catalysis by Ceria and Related Materials*; Trovarelli, A., Ed.; Catalytic Science Series, Vol. 2; Imperial College Press: London, 2002.
- (16) Liu, X.; Zhou, K.; Wang, L.; Wang, B.; Li, Y. *J. Am. Chem. Soc.* **2009**, *131*, 3140–3141.
- (17) Campbell, C. T. *Science* **2005**, *309*, 713–714.
- (18) Salmeron, M.; Schlögl, R. *Surf. Sci. Rep.* **2008**, *63*, 169–199.
- (19) Fleig, J. *Phys. Chem. Chem. Phys.* **2005**, *7*, 2027.
- (20) Esch, F. *Science* **2005**, *309*, 752–755.
- (21) Mogensen, M. *Solid State Ionics* **2000**, *129*, 63–94.
- (22) Murray, E. P.; Tsai, T.; Barnett, S. A. *Nature* **1999**, *400*, 649–651.
- (23) *The CRC Handbook of Solid State Electrochemistry*; CRC Press: Boca Raton, FL, 1997.
- (24) Grass, M. E.; Karlsson, P. G.; Aksoy, F.; Lundqvist, M.; Wannberg, B.; Mun, B. S.; Hussain, Z.; Liu, Z. *Rev. Sci. Instrum.* **2010**, *81*, 053106.
- (25) Whaley, J. A.; McDaniel, A. H.; El Gabaly, F.; Farrow, R. L.; Grass, M. E.; Hussain, Z.; Liu, Z.; Linne, M. A.; Bluhm, H.; McCarty, K. F. *Rev. Sci. Instrum.* **2010**, *81*, 086104.
- (26) Mullins, D.; Overbury, S.; Huntley, D. *Surf. Sci.* **1998**, *409*, 307–319.
- (27) Bluhm, H. *J. Electron Spectrosc. Relat. Phenom.* **2010**, *177*, 71–84.
- (28) Ladas, S.; Kennou, S.; Bebelis, S.; Vayenas, C. G. *J. Phys. Chem.* **1993**, *97*, 8845–8848.

(29) Ertas, G.; Suzer, S. In *Surface Chemistry in Biomedical and Environmental Science*; Blitz, P. J., Gun'ko, V. M., Eds.; Springer: Dordrecht, The Netherlands, 2006; pp 45–58.

(30) El Gabaly, F.; Grass, M.; McDaniel, A. H.; Farrow, R. L.; Linne, M. A.; Hussain, Z.; Bluhm, H.; Liu, Z.; McCarty, K. F. *Phys. Chem. Chem. Phys.* **2010**, *12*, 12138.

(31) Duhm, S.; Heimel, G.; Salzmann, I.; Glowatzki, H.; Johnson, R. L.; Vollmer, A.; Rabe, J. P.; Koch, N. *Nat. Mater.* **2008**, *7*, 326–332.

(32) Xie, Y.; Hikita, Y.; Bell, C.; Hwang, H. Y. *Nat. Commun.* **2011**, *2*, 494.

(33) Vázquez, H.; Dappe, Y. J.; Ortega, J.; Flores, F. J. *Chem. Phys.* **2007**, *126*, 144703.

(34) Schmickler, W.; Santos, E. *Interfacial Electrochemistry*; Springer: Heidelberg, Germany, 2010.

(35) *Chemical Bonding at Surfaces and Interfaces*, 1st ed.; Nilsson, A., Pettersson, L. G. M., Nørskov, J. K., Eds.; Elsevier: Amsterdam, 2008.

(36) Kresse, G.; Hafner, J. *Phys. Rev. B* **1993**, *48*, 13115–13118.

(37) Kresse, G.; Hafner, J. *Phys. Rev. B* **1994**, *49*, 14251–14269.

(38) Kresse, G. *Phys. Rev. B* **1996**, *54*, 11169–11186.

(39) Nolan, M. J. *Phys. Chem. C* **2011**, *115*, 6671–6681.

(40) Li, H.-Y.; Wang, H.-F.; Gong, X.-Q.; Guo, Y.-L.; Guo, Y.; Lu, G.; Hu, P. *Phys. Rev. B* **2009**, *79*, 193401.

(41) Marsman, M.; Kresse, G. *J. Chem. Phys.* **2006**, *125*, 104101.

(42) Zeng, Z.; Ma, X.; Ding, W.; Li, W. *Sci. China Chem.* **2010**, *53*, 402–410.

(43) Butcher, D. R.; Grass, M. E.; Zeng, Z.; Aksoy, F.; Bluhm, H.; Li, W.-X.; Mun, B. S.; Somorjai, G. A.; Liu, Z. *J. Am. Chem. Soc.* **2011**, *133*, 20319–20325.

(44) El Gabaly, F.; McDaniel, A. H.; Grass, M.; Chueh, W. C.; Bluhm, H.; Liu, Z.; McCarty, K. F. *Chem. Commun.* **2012**, *48*, 8338.

(45) Adler, S. B. *Chem. Rev.* **2004**, *104*, 4791–4844.

(46) Vetter, K. *Electrochemical Kinetics: Theoretical and Experimental Aspects*; Academic Press: New York, NY, 1967.

(47) Bockris, J. O. *Modern Electrochemistry*, 2nd ed.; Plenum Press: New York, 1998.

(48) Bluhm, H.; Hävecker, M.; Knop-Gericke, A.; Kiskinova, M.; Schlögl, R.; Salmeron, M. *MRS Bull.* **2007**, *32*, 1022–1030.

(49) NIST Standard Reference Database 71. <http://www.nist.gov/srd/nist71.cfm> (accessed Apr 13, 2013).